Check for updates

Tunable band gap of Bi^{3+}-doped anatase TiO_2 for enhanced photocatalytic removal of acetaminophen under UV-visible light irradiation

Ahmed Alzamly, Fathalla Hamed, Tholkappiyan Ramachandran, Maram Bakiro, Salwa Hussein Ahmed, Shefaa Mansour, Sahar Salem, Khaldiha Abdul al, Nawf Saif Al Kaabi, Mohammed Meetani and Abbas Khaleel

ABSTRACT

A series of Bi^{3+}-doped TiO_2 photocatalysts has been prepared via the propylene oxide (PO) assisted sol-gel method. The effect of Bi^{3+} doping on structural surface morphology and optical properties of the as-prepared photocatalysts was characterized using UV-Visible (UV-Vis) diffuse reflectance spectroscopy, X-ray diffraction, scanning electron microscopy, energy-dispersive X-ray spectroscopy, Brunauer-Emmett-Teller for determination of the specific surface area and porosity, and X-ray photoelectron spectroscopy. Increasing the Bi^{3+} doping percentage up to 10 mole percent, resulted in all as-prepared photocatalysts exhibiting pure anatase phase upon calcination at 400 °C for 3 hours. A red shift in optical band gap measurements was observed with increasing Bi^{3+} ion percent doping, which led to extension of the photocatalysts' activity to the visible region. The enhanced photocatalytic activity for removal of the pharmaceutical compound acetaminophen under UV-Vis light irradiation was demonstrated by comparing bismuth doped as-prepared photocatalysts with pure TiO_2 photocatalysts prepared under the same conditions. Based on experimental conditions, the highest activity was achieved using 10 mole percent Bi^{3+}-doped photocatalyst, where over a period of 4 hours more than 98% acetaminophen removal was achieved.

Key words | acetaminophen, band gap, bi-doped TiO_2, photocatalytic, UV-Vis irradiation

Ahmed Alzamly (corresponding author)
Maram Bakiro
Salwa Hussein Ahmed
Shefaa Mansour
Sahar Salem
Khaldiha Abdul al
Nawf Saif Al Kaabi
Mohammed Meetani
Abbas Khaleel
Department of Chemistry,
UAE University,
P.O. Box 15551, Al-Ain,
UAE
E-mail: *ahmed.alzamly@uaeu.ac.ae*

Fathalla Hamed
Tholkappiyan Ramachandran
Department of Physics,
UAE University,
P.O. Box 15551, Al-Ain,
UAE

INTRODUCTION

Pharmaceutical pollutants tend to be discharged into the aquatic environment from several sources that include: manufacturing facilities (Pérez *et al.* 2017), disposal of various consumer products of a chemical nature (Douziech *et al.* 2018), and hospital waste (Verlicchi *et al.* 2010; Zhang *et al.* 2010). The presence of these pollutants has negatively impacted both humans and aquatic species (Halpern *et al.* 2008; Kostich *et al.* 2014), raising concerns about the effect of the increased level of such pharmaceutical residues on human health and the environment (Jones *et al.* 2005). Acetaminophen, also known as paracetamol, is the most widely used pharmaceutical in the treatment of fever and headache, and consequently is the most common pharmaceutical residue detected in wastewater (Petrie *et al.* 2015). The main concern associated with the excessive use of acetaminophen

This is an Open Access article distributed under the terms of the Creative Commons Attribution Licence (CC BY-NC-ND 4.0), which permits copying and redistribution for non-commercial purposes with no derivatives, provided the original work is properly cited (http://creativecommons.org/licenses/by-nc-nd/4.0/).

doi: 10.2166/wrd.2018.021

Downloaded from http://iwaponline.com/jwrd/article-pdf/9/1/31/523093/jwrd0090031.pdf
by guest

is how easily it accumulates in the aquatic environment due to its characteristics that include high solubility and hydrophilicity (Granberg & Rasmuson 1999). The treatment of such pharmaceutical residue using common chemical treatment processes, e.g. chemical oxidation, results in the production of secondary pollutants resulting from the chemical reaction (Wu *et al.* 2012). Hence, other more environmentally friendly treatment methods need to be explored.

One such method for the environmental remediation of pollutants is the process of photocatalysis, which involves the use of a semiconductor photocatalyst to carry out redox reactions on its surface, speeding up the rate of chemical reactions (Wu *et al.* 1999). When light with photons equal to or greater than the band gap of the semiconductor is absorbed, photo-generated electrons and holes migrate to the surface of the semiconductor where redox reactions take place, by which an effective photocatalyst is one in which the charge couple redox potential is within the photocatalyst's band gap range (Ibhadon & Fitzpatrick 2013). For the conduction band, the bottom energy level regulates the reducing potential of the photoelectrons, whereas the valence band top energy level regulates the oxidizing potential of the photo-generated gaps (Ola & Maroto-Valer 2015). Hence, a suitable semiconductor photocatalyst should have appropriate band gap energy. Other characteristics of an ideal photocatalyst include ease of production (Li *et al.* 2016), stability (Meng *et al.* 2011; Huang *et al.* 2013), cost effectiveness (Zhao & Liu 2008), safety for humans and the environment (Lee *et al.* 2010), easy activation using solar light (Asahi *et al.* 2001), as well as the capability to effectively catalyze reactions (Qu & Duan 2013). This process of photocatalysis has been widely implemented in pollution control for both water and air, wherein it has the capacity to remove waste and degrade toxic substances into non-toxic forms (Chong *et al.* 2010; Luengas *et al.* 2015).

Different photocatalysts have been reported in the literature, including: GaAs, PbS, CdS, ZnO and TiO_2 (Zhang *et al.* 2009; Wang *et al.* 2013; Etacheri *et al.* 2015). Among these photocatalysts, GaAs, PbS, and CdS suffer from instability in aqueous media and are toxic (Gupta & Tripathi 2012). As for ZnO, it exhibits lack of stability when dissolved in water where it produces $Zn(OH)_2$ on the surface of the particles, inactivating the catalyst with time (Daneshvar *et al.* 2007). On the other hand, the characteristics of TiO_2 make it an ideal photocatalyst, as it is cheap (Macwan *et al.* 2011), non-toxic (Choi 2006) and photo-stable in solution (Christy *et al.* 2009). Other characteristics of TiO_2 that are essential for a photocatalyst include high surface area and high porosity, which result in an improved reaction rate because of the improved level of interaction of the reactants with the active sites (Yu *et al.* 2003). As a result, the use of TiO_2 as a photocatalyst has been widely explored in the literature as displaying promise in environmental remediation applications (Pelaez *et al.* 2012).

TiO_2 has three main phases: anatase, rutile and brookite. The anatase phase is the most active form, used in photocatalysis applications (Zhang *et al.* 2000). However, a disadvantage of this photocatalyst is its lack of visible light absorption due to its large band gap energy of 3.2 eV, thus limiting its application under visible light irradiation (Yin *et al.* 2009; Landmann *et al.* 2012). To overcome this drawback, different methods have been reported in the literature to extend its spectral response to visible light, including metal (Fiszka Borzyszkowska *et al.* 2016) and non-metal (Burda *et al.* 2003) doping, coupling of TiO_2 with other semiconductor materials (Liu *et al.* 2007a), fabrication of nanocomposite photocatalysts with different morphologies (Liu *et al.* 2007b; Wang *et al.* 2007; Zhong *et al.* 2014; Chen *et al.* 2017), and dye sensitization (Park *et al.* 2000). Among these methods, doping has been found to be an effective way to extend the light absorption to the visible region by introducing additional energy levels between the valence band and conduction band of the photocatalyst acting as a trap for the charge carriers, facilitating their separation from the bands. This in turn allows more charge carriers to successfully diffuse to the surface of the photocatalyst (Kim *et al.* 2005; Yang *et al.* 2010).

Bismuth based composite oxide semiconductors such as bismuth titanate (Feng Yao *et al.* 2003) show enhanced photocatalytic activity under visible light irradiation, which can be attributed to their narrow band gaps compared to TiO_2. In such a case, band gap reduction is attributed to the hybridized valence band of Bi^{+3} 6S lying above the O 2p and the Ti^{4+} 3d level just below the Bi^{3+} 6p in the conduction band. As a result, band gap energy reduction is assumed to be due to the excitation of a 6S electron of Bi^{3+} into the 3d of Ti^{4+}. This behavior has been observed in other bismuth-based materials such as bismuth vanadate (Huang *et al.* 2014), bismuth

Downloaded from http://iwaponline.com/jwrd/article-pdf/9/1/31/523093/jwrd0090031.pdf
by guest

molybdate (Shimodaira *et al.* 2006) and bismuth tungstate (Zhang & Zhu 2012). In these semiconductors, the hybrid valence bands formed between O 2p and Bi^{3+} 6S levels and conduction band between V; 3d, Mo; 4d and W; 5d orbitals respectively and the Bi^{3+} 6p (Walsh *et al.* 2009). Accordingly, the absorption extends to a longer wavelength due to the excitation of a 6S electron of Bi^{3+} into the d orbital representing the metal ion. Thus, incorporating Bi^{3+} ion into the TiO_2 band structure is anticipated to have a similar effect, shifting light absorption to the longer wavelengths, i.e. visible region. This in turn induces high photocatalytic activity under visible light irradiation of the bismuth doped photocatalysts.

In this work, we present a facile propylene oxide (PO) assisted sol-gel preparation of TiO_2 and bismuth-doped TiO_2. The performance of the as-prepared photocatalysts was evaluated by the removal of acetaminophen from an aqueous solution over a period of 4 hours under UV and visible light irradiation.

METHOD

Materials

Titanium (IV) n-butoxide ($Ti(O^nBu)_4$, 97%), $Bi(NO_3)_3.5H_2O$, 2-propanol (*i*-PrOH, 99.7%), hydrochloric acid (HCl, 37%), acetylacetone (acac, 99.3%) and propylene oxide (PO, 99%) were purchased from Sigma Aldrich and used as received. All chemicals were used without further purification. Solutions were prepared using doubly distilled water passed through a Milli-Q apparatus.

Preparation of the photocatalysts

Preparation of TiO_2

The TiO_2 photocatalyst was prepared through mixing $Ti(O^nBu)_4$ solution and the hydrolysis solution that were prepared as indicated below.

$Ti(O^nBu)_4$ solution: The TiO_2 photocatalyst was synthesized using $Ti(O^nBu)_4$, 2-propanol (*i*-PrOH) used as solvent, acetylacetone (acac) as the complexing agent and PO as the gelation promoter using the sol-gel method at room temperature. In a typical synthesis, $Ti(O^nBu)_4$ was dissolved in *i*-PrOH in a *i*-PrOH:$Ti(O^nBu)_4$ v/v ratio of 5:1 where acac was added in a molar ratio $Ti(O^nBu)_4$: acac of 1:2. The prepared solution was kept under constant stirring for 2 hours followed by the addition of PO where the PO: $Ti(O^nBu)_4$ molar ratio was 10:1.

The hydrolysis solution: The hydrolysis solution was made by mixing distilled water and *i*-PrOH (*i*-PrOH:H_2O, 1:20) where the H_2O:$Ti(O^nBu)_4$ molar ratio was 10:1. The hydrolysis reaction was initiated through the addition of $Ti(O^nBu)_4$ solution to the hydrolysis solution drop wise under vigorous stirring. The pH of the final solution was adjusted to pH = 2 through the addition of 37% HCl. This reaction mixture was stirred for an additional period of 3 hours and then aged for a few days for the formation of the gel. After drying, powder was air-calcinated at 400 °C for 3 hours.

Preparation of Bi^{3+}-doped TiO_2 photocatalysts

For the preparation of the Bi^{3+}-doped TiO_2 photocatalysts, the same procedure as that for the preparation of TiO_2 photocatalyst was implemented, where molar amounts of Bi were added. Samples of 1%, 3%, 5%, and 10% of Bi-doped TiO_2 were prepared, respectively, where Bi was first dissolved in a *i*-PrOH:H_2O v/v ratio of 1:5 followed by the addition of a few drops of 37% HCl. The Bi^{3+} solution was then added to the $Ti(O^nBu)_4$ solution prior to the PO addition. Finally, hydrolysis solution was added dropwise under vigorous stirring. All as-prepared Bi-doped photocatalysts were air-calcinated at 400 °C for 3 hours.

Characterization of the photocatalysts

UV-Visible diffuse reflectance spectroscopy (UV-Vis DRS)

UV-Vis diffuse reflectance spectroscopy measurements were obtained using a Shimadzu UV-3600 UV-Vis spectrophotometer from 200 to 800 nm where the baseline was corrected using $BaSO_4$ as a reference standard. The band gap energies were calculated using the results from the spectra and the application of the Tauc Plot method (Tauc 1970). The band gap was calculated considering that these photocatalysts were indirect semiconductors and using Equation (1), where α, E_g, h, ν, A, n represent the absorption

Downloaded from http://iwaponline.com/jwrd/article-pdf/9/1/31/523093/jwrd0090031.pdf
by guest

coefficient, band gap, Planck's constant, frequency of light, a constant, and the number characterizing transition for indirect semiconductor materials ($n = 1/2$ for TiO_2), respectively (Zhang *et al.* 2014).

$$(\alpha h\nu)^{1/n} = A\,(h\nu - E_g) \quad (1)$$

According to the above equation, through the construction of a plot of $(\alpha h\nu)^2$ versus $h\nu$ (eV), the band gap energy E_g can be obtained by extrapolating a line through the steep linear part of the curve to the hν axis as shown in Figure 1, whereas the band gap values are tabulated in Table 1.

X-ray diffraction (XRD)

X-ray diffraction characterization was performed using a Shimadzu-6100 powder XRD diffractometer with Cu-Kα radiation. The working voltage and current of the X-ray tube were 40 kV and 40 mA respectively, where $\lambda =$ 1.542 Å. The diffraction data were collected in the 2θ angle range of 20–80 degrees at a rate of 2 degrees/min. Figure 2 displays the XRD results for all the photocatalysts used in this study.

Scanning electron microscopy (SEM) and energy-dispersive X-ray spectroscopy (EDS)

Scanning electron microscope images and energy-dispersive X-ray spectroscopy were obtained using JEOL JSM–6010LA. After film preparation on ITO-coated glass, samples were rinsed and allowed to dry. Images and data were then collected at accelerating voltage of 20 kV as presented in Figures 3 and 4 and Table 1.

Specific surface area and porosity

Surface area and porosity were characterized using N_2 adsorption at 77 K using a Quantachrome Autosorb-1 volumetric gas sorption instrument. Before measurements, samples were degassed at 150 °C for 1 hour. Brunauer-Emmett-Teller (BET) theory was used to calculate surface area, and pore size distributions were determined by the Barett-Joyner-Halenda (BJH) model based on the desorption branch of the N_2 isotherms. Specific surface area and porosity data analysis are presented in Table 1.

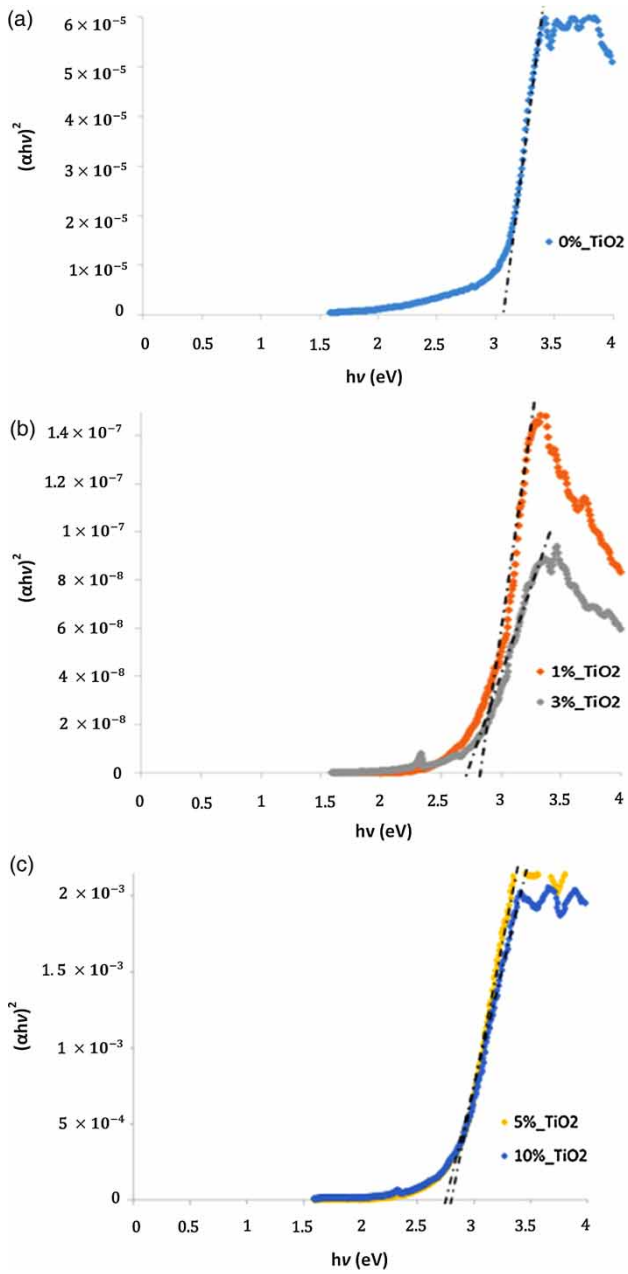

Figure 1 | UV-Vis diffuse reflectance spectra of pure (a) and different % Bi^{3+} doped TiO_2 as-prepared photocatalysts (b, c).

X-ray photoelectron spectroscopy (XPS)

X-ray photoelectron spectroscopy measurements of all as-prepared photocatalysts were performed using the Kratos

Downloaded from http://iwaponline.com/jwrd/article-pdf/9/1/31/523093/jwrd0090031.pdf
by guest

Table 1 | Physical structure parameters of as-prepared photocatalysts

Catalyst (% Bi doping)	Band gap energy (eV)	S_{BET} ($m^2\ g^{-1}$)	Pore size (nm)	V_{pores} ($cm^3\ g^{-1}$)	Crystalline size (nm)	Apparent rate constant (h^{-1})	Lattice constant (Å)		EDS (Atom %)		
							a = b	c	Ti	O	Bi
0	3.08	125.36	7.17	0.138	73	0.58	3.795	9.786	30.18	69.82	0
1	2.91	33.78	7.74	0.0595	105	0.63	3.793	9.754	30.61	69.12	0.27
3	2.87	39.27	7.92	0.139	112	0.73	3.796	9.773	27.27	71.78	0.95
5	2.84	42.86	11.87	0.120	125	0.72	3.791	9.642	29.93	68.75	1.31
10	2.80	60.00	11.29	0.181	131	0.97	3.776	9.345	30.25	68.19	1.56

Axis Ultra DLD spectrometer (Kratos Analytical Ltd, Manchester, UK) with Al $K_{\alpha 1}$ X-ray source. The energy of an X-ray photon of 1.486 keV with pass energy of 160 eV was used for the survey spectrum and 20 eV for narrow scans. All spectra were collected at a 54° take-off angle and analyzed area of ($700 \times 300\ \mu m$) using the combination of electrostatic and magnetic lens (hybrid mode). The C 1 s peak from adventitious hydrocarbon at 284.8 eV was used as an energy reference to correct for charging. Surface charging effects were minimized using a charge balance operating at 3.6 V and 1.8 V maintained as filament bias. During XPS analysis, sample charging was neutralized using an electron flood gun. All spectra were recorded under ultra-high vacuum conditions below 5×10^{-10} mbar. All data processing was carried out using the Casa XPS software (Casa Software Ltd) package. For calculation of the elemental composition of the prepared photocatalysts, the determined areas under the peaks were normalized using the Scofield sensitivity factors. For data evaluation, the background of the Auger photoelectron peaks was subtracted by applying a Shirley-type of background and the data were curve-resolved using an 80% Gaussian/20% Lorentzian sum.

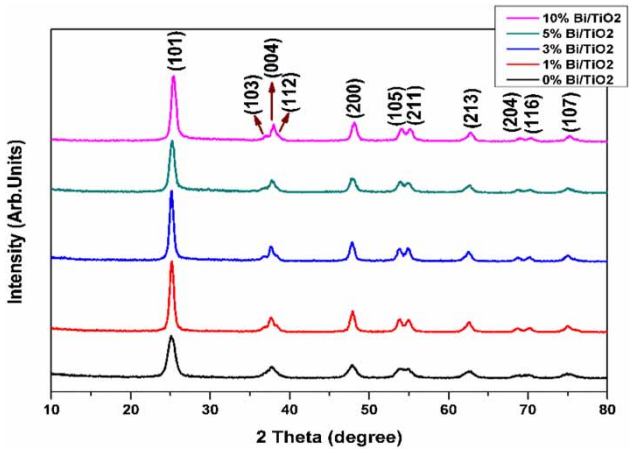

Figure 2 | XRD chart of the as-prepared % Bi doped TiO_2 photocatalysts compared with pure TiO_2.

Photocatalytic activities

The photocatalytic evaluation of Bi^{3+}-doped TiO_2 as-prepared photocatalysts in the removal of acetaminophen in aqueous solution was performed using a Luzchem Photoreactor (Mod. LZC-1, Luzchem Research Inc., ON, CAN) equipped with two UVA lamps centered at ~350 nm, two UVB lamps centered at ~300 nm with a peak of 313 nm, two UVC (254 nm) germicidal lamps, and seven cool white fluorescent tubes. Temperature was kept constant at 25 °C for all the reactions. In a typical photocatalytic run, powdered photocatalyst in the amount of 0.1 gL^{-1} was suspended in aqueous solution of 10^{-4} M acetaminophen in a 100-mL quartz beaker. The suspension was magnetically stirred in the dark over 30 min to achieve a complete adsorption/desorption equilibrium and then it was irradiated with a UV-Vis light source. The light intensity was measured using a digital light meter (TES-1330A) and it was 11,460 lux (44 W/cm^2). Aliquots of the reaction medium were periodically sampled and filtered using a polytetrafluoroethylene (PTFE) membrane filter (Millipore, 0.22 μm) prior to analysis. The acetaminophen concentration was measured employing a spectrophotometric method by using a double beam UV-Vis SPECORD 210 PLUS spectrophotometer and following the decrease in the absorbance of acetaminophen at 250 nm over time definite intervals.

Downloaded from http://iwaponline.com/jwrd/article-pdf/9/1/31/523093/jwrd0090031.pdf
by guest

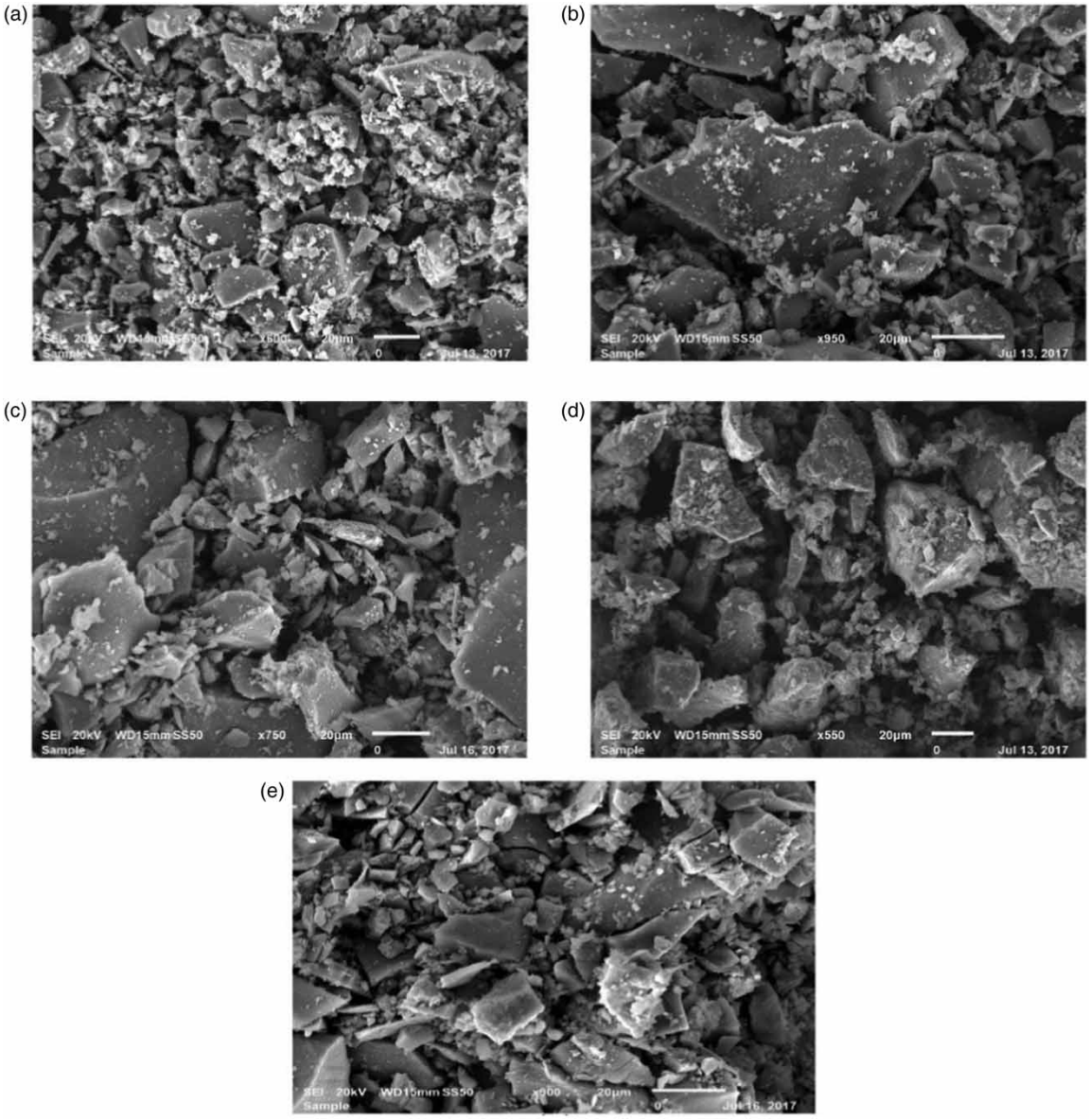

Figure 3 | SEM 20 (μm) images of different % Bi-doped TiO_2 photocatalysts. (a) 0%, (b) 1%, (c) 3%, (d) 5% and (e) 10%.

RESULTS AND DISCUSSION

Characterization results

Band gap UV-Vis DRS

Tauc plots of the UV-Vis DRS spectra of the pure TiO_2 and bismuth-doped TiO_2 as-prepared photocatalysts are presented in Figure 1. Pure TiO_2 exhibited a direct allowed band gap of 3.08 eV. On the other hand, all bismuth doped as-prepared photocatalysts showed quite similar light absorption shifts towards the visible region of the spectrum, with the lowest band gap of 2.8 eV for the 10% Bi^{3+}-doped TiO_2 photocatalyst, i.e. a red shift of approximately 40 nm from that of pure TiO_2. This red shift observed for all doped as-prepared photocatalysts can be attributed to the presence of bismuth ion within the TiO_2 lattice and lack of presence as a secondary

Downloaded from http://iwaponline.com/jwrd/article-pdf/9/1/31/523093/jwrd0090031.pdf
by guest

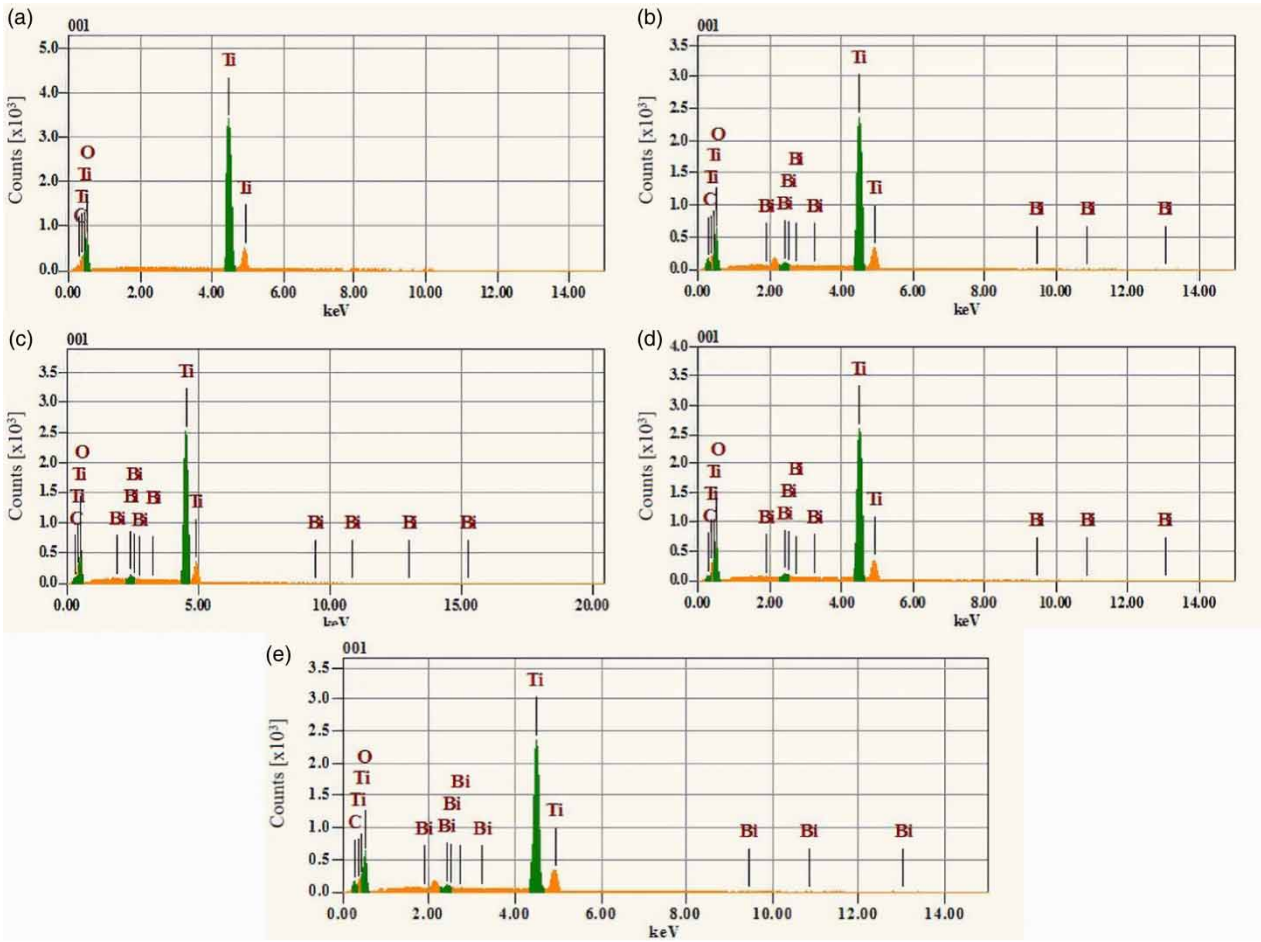

Figure 4 | EDS spectrum of Bi-doped TiO_2. (a) 0%, (b) 1%, (c) 3%, (d) 5% and (e) 10% samples, insert spectrum shows the elemental composition of corresponding EDS spectrum.

phase as indicated solely by the XRD spectra presented in Figure 2.

XRD

Figure 2 displays the XRD patterns of the as-prepared pure and bismuth-doped TiO_2 photocatalysts with varying amounts of Bi^{3+} dopant. From the figure, it can be observed that the peaks for the doped TiO_2 samples coincide with those of the pure TiO_2 in which all the patterns displayed indicate the presence of the pure anatase TiO_2 phase with no peaks corresponding to another phase or newly formed lattice structure. Furthermore, the fact that there was no observed shift in the diffraction angles of the XRD peaks indicates that doped Bi^{3+} ions did not cause any changes in the phase composition to the TiO_2 lattice structure at the studied doping level. The fact that Bi^{3+} species were incorporated into the TiO_2 lattice without changing its phase does not necessarily rule out the possibility that bismuth may present as a separate phase onto the surface of TiO_2, as in the case of Bi_2O_3 as claimed by Wang *et al.* (2008). Similar results have been reported by Yang *et al.* in the work performed on TiO_2 photocatalysts prepared through coupling with Bi_2O_3 and doping with Si (Yang *et al.* 2014). However, in this study, the XRD peaks of the as-prepared photocatalysts corresponding to Bi_2O_3 were not found even when samples were calcinated at 700 °C. Therefore, the absence of this compound is not conclusive, since it is believed that presence of minor amounts of Bi_2O_3 cannot be detected by XRD (Ji *et al.* 2009).

Using the XRD data, the average crystalline sizes of the as-prepared photocatalysts can be calculated by applying the

Downloaded from http://iwaponline.com/jwrd/article-pdf/9/1/31/523093/jwrd0090031.pdf
by guest

Debye-Scherrer formula on the anatase (101) diffraction peaks (Patterson 1939).

$$D = \frac{K\lambda}{\beta \cos\theta} \quad (2)$$

where D is the crystalline size, λ the wavelength of X-ray radiation (0.1541 nm), K a constant 0.89, and β the peak width (in radians) at half maximum height after the subtraction of the equipment broadening, $2\theta = 25.4$ for anatase phase of TiO_2. From the XRD results, the intensity of this characterized peak increased whilst becoming narrower as the mol % of Bi^{3+} doping was increased. In general, the crystal size of the as-prepared photocatalyst increased with increase in mol % of Bi dopant. The results of the crystalline size in nm are presented in Table 1.

The lattice constants of pure and Bi^{3+}-doped as-prepared TiO_2 photocatalysts were calculated using the formula,

$$\frac{1}{d^2} = \frac{h^2 + k^2}{a^2} + \frac{l^2}{c^2} \quad (3)$$

where d is the interplanar spacing in XRD pattern, a and c are the lattice constants in angstrom (Å) and h, k and l are the Miller indices. The calculated values of lattice constant (a = b, and c) for the pure and Bi^{3+}-doped TiO_2 as-prepared photocatalysts are presented in Table 1. The values are in good agreement with the literature values of a = b = 3.785 Å and c = 9.504 Å for pure TiO_2 anatase nanoparticles reported by Milićević *et al.* (2017). Moreover, these values were found to decrease with increasing concentration of Bi^{3+} ions in the as-prepared TiO_2 anatase photocatalysts. This can be explained based on the variation in the ionic radius of Bi^{3+} (0.74 Å) and Ti^{4+} (0.68 Å) in the as-prepared pure and Bi^{3+}-doped TiO_2 photocatalysts, thereby affecting the unit cell and thus resulting in the smaller lattice constants (Li *et al.* 2004; Štengl & Bakardjieva 2010).

SEM

SEM images of pure and Bi^{3+}-doped as-prepared photocatalysts are depicted in Figure 3; the pure and bismuth-doped TiO_2 photocatalyst particles seem to be irregular in shape. These particles displayed a rock-like morphology, where the sizes of the particles of the doped samples seemed to be larger than the un-doped sample under the same magnification. This can be attributed to the presence of particle agglomeration. Similar agglomeration results were reported by Aware & Jadhav (2016) in the work performed on the doping of TiO_2 nanoparticles with zinc using the same method used in the current study, the sol-gel method.

EDS analysis

EDS analysis was used to investigate the quantitative chemical composition for the constituent elements of pure and bismuth-doped TiO_2 as-prepared photocatalysts. Figure 4(a)–4(e) show the binding energy (BE) (keV) in the x-axis versus intensity of X-rays (counts) in the y-axis of the EDS analysis spectrum of as-prepared Bi^{3+}-doped TiO_2 photocatalysts. Based on the EDS spectra, the existence of all corresponding elements, i.e. the peaks of Bi, Ti and O, respectively, present in the as-prepared photocatalysts were confirmed. A carbon peak is also present in the EDS spectra, which is due to the use of carbon tape during analysis. Moreover, the increased carbon content in the EDS spectra may also be attributed to possible contamination due to the hydrocarbon used in the preparation method. Hence, it is tempting to say that the presence of carbon does not dramatically affect as-prepared photocatalysts' performance, since it is present in all photocatalysts in almost similar amounts. No additional impurity peaks were detected, which confirms phase purity of the as-prepared photocatalysts, as further supported by XRD and XPS analysis.

N_2 adsorption-desorption analysis

The N_2 adsorption-desorption isotherms for the pure and Bi^{3+}-doped TiO_2 as-prepared photocatalysts are presented in Figure 5, with the surface area, pore size and volume of the pores as presented in Table 1. All as-prepared photocatalysts were characterized by type IV isotherms, which indicates the presence of mesoporous material. The surface areas for the 1%, 3%, 5% and

Downloaded from http://iwaponline.com/jwrd/article-pdf/9/1/31/523093/jwrd0090031.pdf
by guest

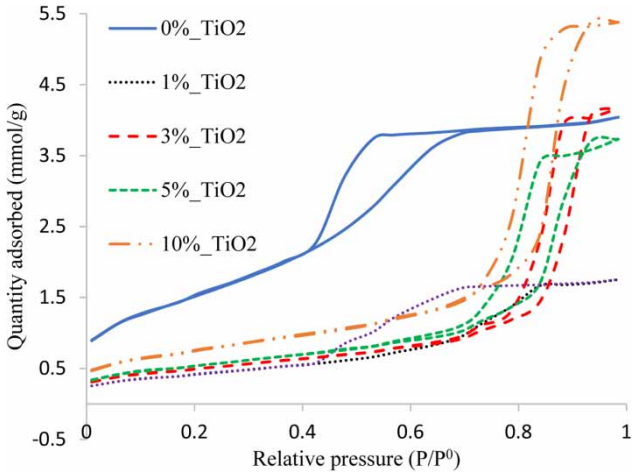

Figure 5 | BET isotherms of un-doped and % Bi-doped TiO_2 photocatalysts.

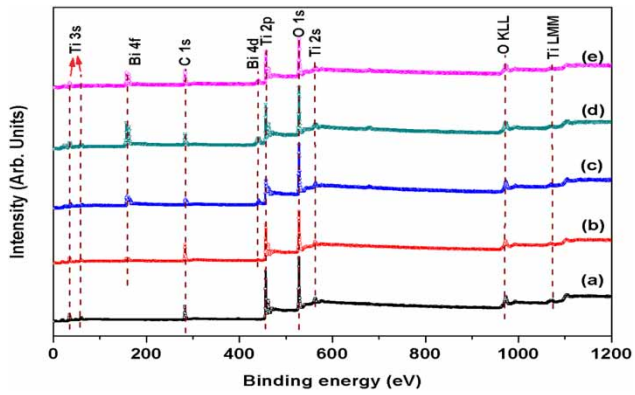

Figure 6 | XPS wide spectrum of synthesized Ti1-xBixO2 (a) x = 0, (b) x = 0.01, (c) x = 0.03, (d) x = 0.05, (e) x = 0.10 samples.

10% Bi-doped photocatalysts were reported at 33.78, 38.27, 42.86 and 60 m^2/g respectively, compared to the pure TiO_2 photocatalyst's surface area of 125.3 m^2/g. According to Table 1, the change caused by Bi^{3+} doping is clear in the 10 mol % Bi-doped photocatalyst exhibiting the highest surface area (60 m^2/g). Moreover, as Bi^{3+} dopant increased, the pore size became larger and the surface area was reduced to a large extent compared with pure TiO_2.

XPS analysis

The elemental composition and valence state of the as-prepared photocatalysts were analyzed by XPS study. The XPS results are presented in Figure 6 and Table 2. The elements Ti, Bi and O in the as-prepared photocatalysts were confirmed in the wide spectrum. It also shows carbon; the high C 1 s content is due to the hydrocarbon contamination introduced from the laboratory environment as shown from EDS analysis. Thus, the observed C 1 s peak was used as an energy reference for determining the peak positions of core level spectra.

For more information about the valence state of titanium and bismuth ions – Ti 2p and Bi 4f – present in the as-prepared photocatalysts, high-resolution spectra were analyzed with respect to Bi^{3+} doping level as shown in Figures 7 and 8. Table 3 displays the fitted peak position corresponding to the BE values of Ti 2p spectra using the Lorentzian-Gaussian curve fitting method. For the pristine TiO_2, Ti 2p peak is distinguishable as two peaks at 462.32 eV for $2p_{3/2}$ and 456.59 eV for $2p_{1/2}$, which

Table 2 | Data obtained from wide XPS spectra for Ti1-xBixO2 (x = 0, x = 0.01, x = 0.03, x = 0.05, x = 0.10)

Sample	Peak	Position (eV)	Area	% Atomic Conc.[a]
x = 0	O 1s	528.00	1,860.09	45.21
	C 1s	283.00	1,541.59	37.47
	Ti 2p	456.50	712.881	17.33
x = 0.01	Bi 4f	162.50	0.559001	0.01
	Ti 2p	456.50	544.509	13.45
	O 1s	528.00	1,640.05	40.52
	C 1s	283.00	1,862.03	46.01
x = 0.03	Bi 4f	157.50	114.038	2.84
	Ti 2p	457.00	754.015	18.76
	O 1s	528.00	1,841.17	45.81
	C 1s	283.50	1,310.07	32.59
x = 0.05	O 1s	528.00	1,688.17	44.56
	C 1s	283.00	1,249.55	32.98
	Ti 2p	456.50	711.049	18.77
	Bi 4f	157.00	139.736	3.69
x = 0.10	O 1s	528.00	1,488.07	39.73
	C 1s	283.00	1,630.95	43.55
	Ti 2p	456.50	547.426	14.62
	Bi 4f	157.00	78.8011	2.10

[a]Percentage contribution of each peak to the total number of counts in Ti 2p, Bi 4f, O 1 s and C 1 s peak.

Downloaded from http://iwaponline.com/jwrd/article-pdf/9/1/31/523093/jwrd0090031.pdf
by guest

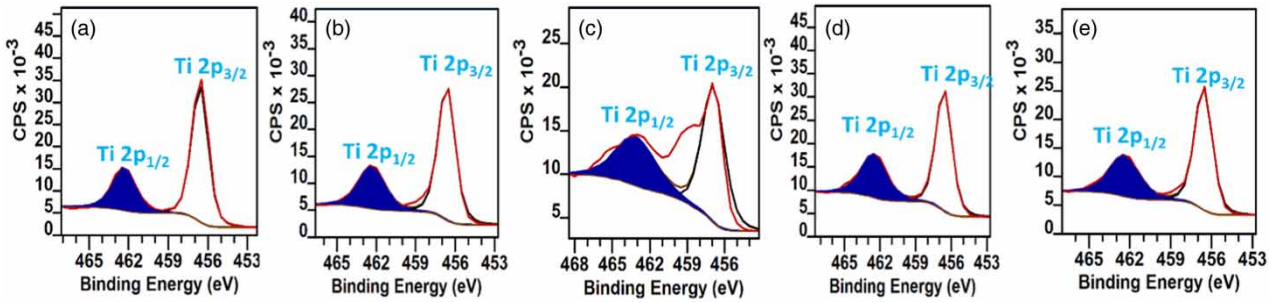

Figure 7 | XPS wide spectrum of synthesized Ti1-xBixO2 (a) x = 0, (b) x = 0.01, (c) x = 0.03, (d) x = 0.05, (e) x = 0.10 samples.

correspond to the characteristics peak of Ti^{4+} ion (Bapna *et al.* 2011). After doping bismuth into the TiO_2, the deconvolution of these peaks shifted towards lower binding energies of about 0.17 eV and peak width increased, indicating a small contribution of Ti^{3+} ion present in the sample. The shifts of these peaks are consistent with what was previously reported by Liu *et al.* (2012). These results may indicate an oxygen deficiency in TiO_2 lattice (Hamdy *et al.* 2012). It is conceivable that bismuth cations are substituted for Ti ion in the $Ti_{1-x}Bi_xO_2$ matrix, because of the decreased Ti 2p peak area in comparison to the pure counterpart.

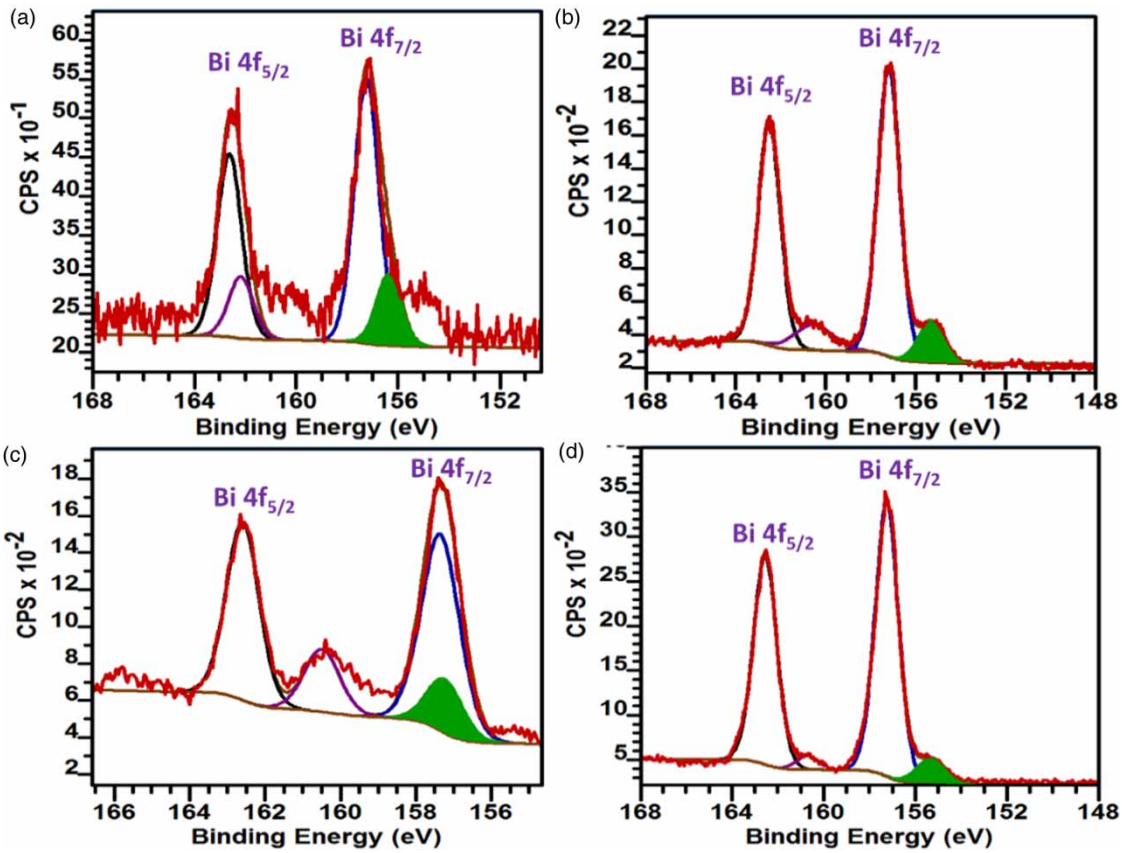

Figure 8 | XPS wide spectrum of synthesized Ti1-xBixO2 (a) x = 0.01, (b) x = 0.03, (c) x = 0.05, (d) x = 0.10 samples.

Downloaded from http://iwaponline.com/jwrd/article-pdf/9/1/31/523093/jwrd0090031.pdf
by guest

Table 3 | Data obtained from high resolution Ti 2p XPS spectra for Ti1-xBixO2 (x = 0, x = 0.01, x = 0.03, x = 0.05, x = 0.10) samples

Sample	Ti $2p_{3/2}$ BE[x] (eV)	Ti $2p_{3/2}$ FWHM[y] (eV)	Ti $2p_{3/2}$ Area (%)	Ti $2p_{1/2}$ BE[x]	Ti $2p_{1/2}$ FWHM[y] (eV)	Ti $2p_{1/2}$ Area (%)	[z]ΔE Ti 2p
x = 0	458.65	1.45	69.34	464.32	2.13	30.66	5.67
x = 0.01	458.59	1.54	67.06	464.24	2.38	32.94	5.65
x = 0.03	458.47	2.12	63.63	464.21	3.41	36.37	5.74
x = 0.05	458.41	1.58	62.90	464.16	2.61	37.10	5.75
x = 0.10	458.29	1.59	40.10	464.11	2.61	59.90	5.82

[x]Binding energies, [y]full width at half maximum and [z]ΔE Ti 2p is the binding energy difference between Ti $2p_{3/2}$ and Ti $2p_{1/2}$ peaks.

It is seen from Figure 8 that the Bi 4f peak is split into two peaks located at ~159.06 eV and ~164.41 eV corresponding to Bi $4f_{5/2}$ and Bi $4f_{7/2}$ peaks, as fitted by the Gaussian-Lorentzian product function after Shirley-type background subtraction. Both are mainly assigned to Bi-O bonds. Spin orbital splitting energy of the Bi 4f doublet is equal to ~5.35 eV, which is a slight increase of about 0.15 eV with increase in the bismuth doping content x in the sample. Furthermore, each of the Bi $4f_{5/2}$ and Bi $4f_{7/2}$ peaks could be fitted by two sub-peaks. The sub-peaks located at 159.19 and 158.24 eV are assigned to Bi $4f_{7/2}$-O, whereas 166.5 and 164.62 eV are of Bi $4f_{5/2}$-O bonds for Bi^{3+} (Mekki *et al.* 1996). Table 4 displays the fitted Bi 4f XPS peak of the samples.

Table 4 | Fitting parameters of deconvoluted Bi 4f XPS spectra for Ti1-xBixO2 (x = 0.01, x = 0.03, x = 0.05, x = 0.10) samples

	Bi $4f_{7/2}$							Bi $4f_{5/2}$						
	Bi $4f_{7/2}$(1)			Bi $4f_{7/2}$(2)				Bi $4f_{5/2}$(1)			Bi $4f_{5/2}$(2)			
Sample	B.E[x]	FW[y]	A[z]	B.E[x]	FW[y]	A[z]	ΔE1	B.E[x]	FW[y]	A[z]	B.E[x]	FW[y]	A[z]	ΔE2
x = 0.01	159.19	1.36	176.107	158.24	1.91	60.914	0.95	166.50	1.45	164.954	164.62	1.81	35.0319	1.88
x = 0.03	160.00	3.79	1,115.16	158.35	1.57	641.652	1.65	166.54	2.76	584.831	164.79	1.73	511.807	1.75
x = 0.05	159.21	1.62	1,999.34	158.20	1.72	71.3654	1.01	166.62	1.58	1,271.75	164.09	1.35	232.819	2.53
x = 0.10	159.18	1.49	1,022.83	158.48	1.74	99.6585	0.7	166.47	1.53	810.443	164.53	1.43	57.468	1.94

[x]Binding energies, [y]full width at half maximum, [z]corresponding area of the peaks, and ΔE1 is the binding energy between Bi $4f_{7/2}$(1) and Bi $4f_{7/2}$(2) whereas ΔE2 is the binding energy between Bi $4f_{5/2}$(1) and Bi $4f_{5/2}$(2).

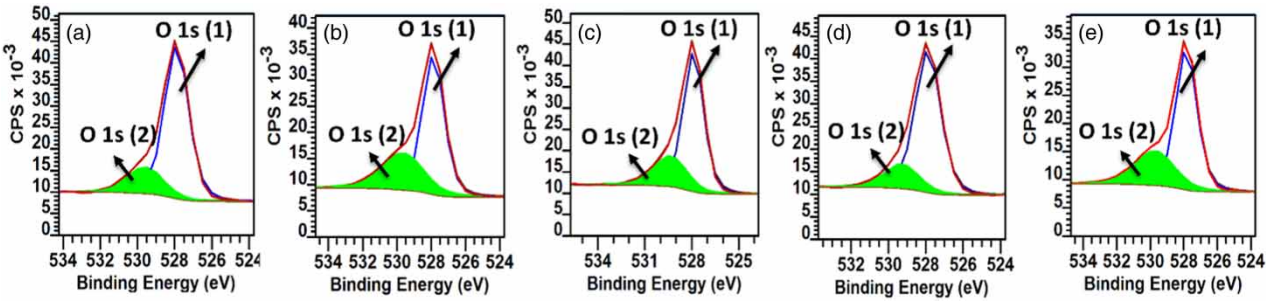

Figure 9 | Deconvolution O 1 s XPS spectra of synthesized Ti1-xBixO2 (a) x = 0, (b) x = 0.01, (c) x = 0.03, (d) x = 0.05, (e) x = 0.10 samples.

Downloaded from http://iwaponline.com/jwrd/article-pdf/9/1/31/523093/jwrd0090031.pdf
by guest

Table 5 | Data obtained from high resolution O 1 s XPS spectra for Ti1-xBixO2 (x = 0, x = 0.01, x = 0.03, x = 0.05, x = 0.10) samples

Sample	O 1 s (1) (eV) BE[x]	FWHM[y]	Area (%)	O 1 s (2) (eV) BE[x]	FWHM[y]	Area (%)	[z] ΔO 1 s
x = 0	529.89	1.53	4,430.84	531.58	2.24	1,113.13	1.69
x = 0.01	529.63	1.48	3,229.49	531.65	2.87	1,640.25	2.02
x = 0.03	529.79	1.51	4,049.25	531.37	2.48	1,442.86	1.58
x = 0.05	529.58	1.59	4,101.56	531.26	2.12	927.752	1.68
x = 0.10	529.84	1.49	3,038.75	531.74	2.78	1,376.96	1.9

[x]Binding energies, [y]full width at half maximum and [z]ΔO 1 s is the difference in binding energies between O 1 s (1) and O 1 s (2) peaks in (eV).

Figure 9 and Table 5 show the O 1 s XPS peak of the $Ti_{1-x}Bi_xO_2$ sample. The O 1 s XPS spectra are well fitted into two peaks situated at 529.88 eV and 531.57 eV. The BE at 529.88 eV is attributed to the contribution of crystal lattice oxygen, whereas the BE at 531.57 eV is called a shoulder peak, which arises due to chemisorbed oxygen species on the surface of samples (Xu *et al.* 2008). Based on the above results, XPS observations confirm that no

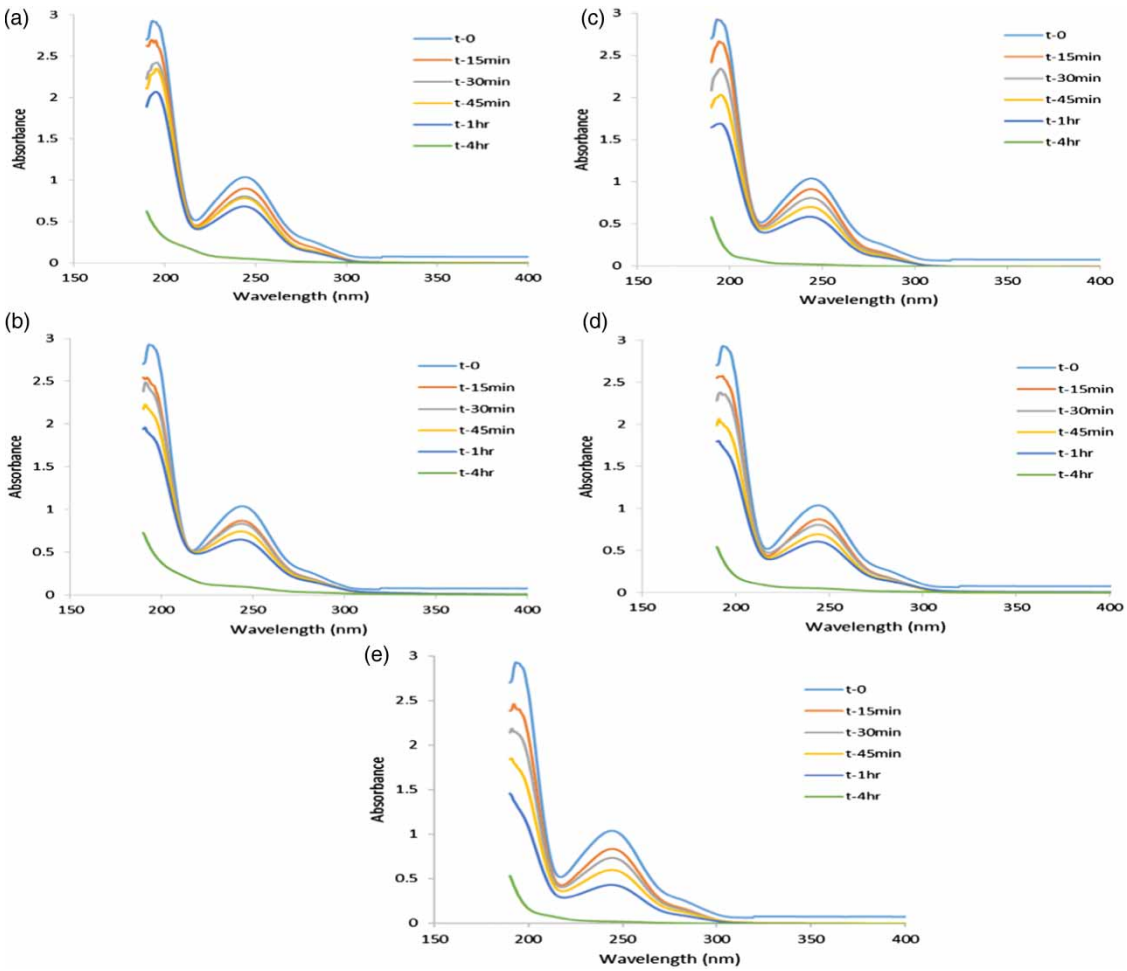

Figure 10 | UV-Vis removal of acetaminophen from aqueous solutions of different % Bi^{3+}-doped TiO_2 photocatalysts. (a) 0%, (b) 1%, (c) 3%, (d) 5% and (e) 10%.

Downloaded from http://iwaponline.com/jwrd/article-pdf/9/1/31/523093/jwrd0090031.pdf
by guest

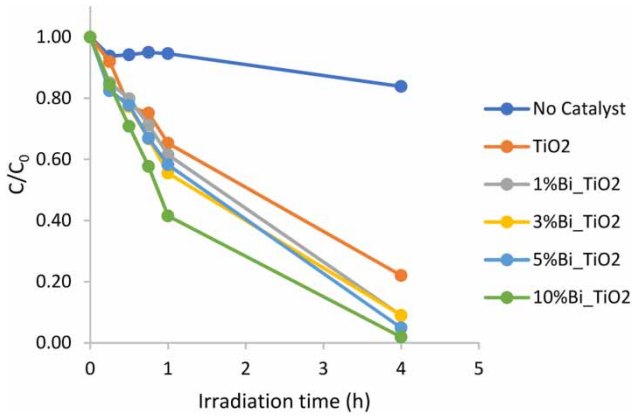

Figure 11 | Variation of the concentration of acetaminophen over time under UV-Vis irradiation in the presence of different % Bi^{3+} dopants.

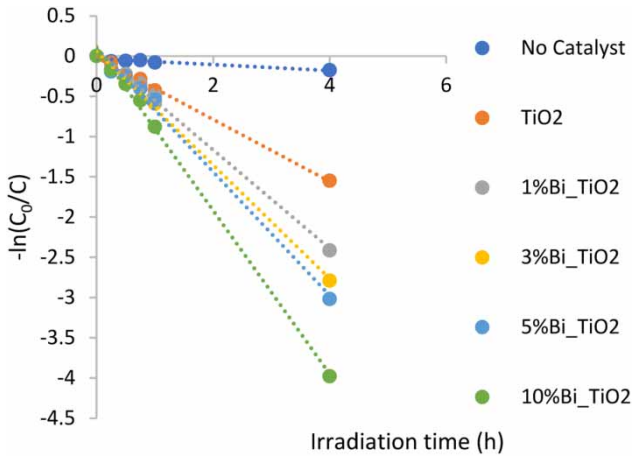

Figure 12 | Kinetic plot of $-\ln(C_0/C)$ over time for the disappearance of acetaminophen for the different % Bi^{3+}-doped TiO_2.

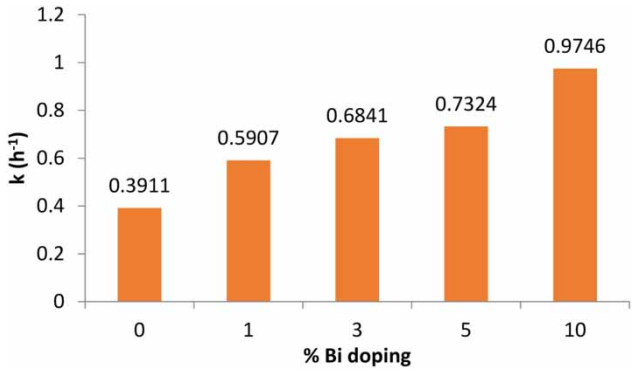

Figure 13 | Rate constants for kinetic studies of different % Bi^{3+}-doped photocatalysts.

additional/impurity phase was formed, which further supports the EDS and XRD results.

PHOTOCATALYTIC ACTIVITY

The photocatalytic activity of the as-prepared pure and Bi^{3+}-doped photocatalysts was evaluated in terms of their rate of acetaminophen removal from aqueous solution at pH = 5. The results indicated a direct relation between the percentages of Bi^{3+}-doped TiO_2 and the removal rate of the pharmaceutical as presented in Figures 10–13. Upon comparing the photocatalytic removal of acetaminophen, 10 mol % Bi^{3+}-doped photocatalyst's performance exceeded that of the pure as-prepared TiO_2. Figure 11 presents the graph of C/C_o vs. time by which the variation of the concentration of acetaminophen is observed for the different photocatalysts under UV-Vis light with irradiation time up to 4 hours. Although the surface areas of as-prepared Bi-doped photocatalysts are significantly lower than that of pure TiO_2, their enhanced photocatalytic activities might be due to their suitable band gaps absorption that occurs in the visible light region.

The photocatalytic removal of acetaminophen follows pseudo-first-order reaction kinetics for the concentration range of the present study (Dalida *et al.* 2014). As a result, the variation in $-\ln(C_o/C)$ as a function of irradiation time is reported in Figure 12, by which the rate constants were calculated in Figure 13 and listed in Table 1. The observed photocatalytic activity of Bi^{3+}-doped as-prepared photocatalysts follows the order: 10 > 5 > 3 > 1> pure TiO_2, where enhanced removal of acetaminophen from solution under UV-Vis light irradiation is mainly ascribed to the Bi^{3+} doping. The doping with Bi^{3+} ion into the lattice of TiO_2 reduces the band gap energy. Therefore, the excitation energy is extended to the visible region. In our studied doping range, results from photocatalytic experiments are found to be in agreement with that of UV-Visible diffuse reflectance spectra analysis. Generally, the increase in mol % of Bi^{3+} doping led to a red shift increase, thereby resulting in higher photocatalytic activity. Moreover, as evident from the enhanced photocatalytic performance of Bi^{3+}-doped photocatalysts in comparison to the un-doped photocatalysts, the presence of Bi^{3+} ions

Downloaded from http://iwaponline.com/jwrd/article-pdf/9/1/31/523093/jwrd0090031.pdf
by guest

in the TiO_2 lattice significantly influences photoactivity by reducing charge carrier recombination rates during the irradiation process.

CONCLUSION

In conclusion, mesoporous Bi^{3+}-doped anatase TiO_2 photocatalysts have been prepared using the PO assisted sol-gel method. The characterization results displayed suggest that the Bi^{3+} ion conceivably caused substitutional changes to the crystal lattice without altering its anatase phase. All doped as-prepared photocatalysts were found to have enhanced photocatalytic activities towards the removal of acetaminophen in aqueous solution under UV-Vis solar light irradiation compared to pure TiO_2. The enhanced photocatalytic activity indicated that Bi^{3+} doping into the TiO_2 enhanced the visible light absorption, as compared to the pure TiO_2. The rate of the photocatalytic reactions was found to depend mainly on the percent doping of Bi^{3+} ion, with the highest activity achieved for the highest doping percent of 10% added within the range of this study.

ACKNOWLEDGEMENTS

This research project was financially supported by the United Arab Emirates University 'SURE Plus' (grant no. 31S292, Ahmed Alzamly). The authors of this paper would like to acknowledge Mr Bassam Al-Hindawi for his assistance and guidance in the performance of BET analysis as well as Ms Afra Gharib Al-Blooshi for her cooperation with obtaining the SEM images.

REFERENCES

Asahi, R., Morikawa, T., Ohwaki, T., Aoki, K. & Taga, Y. 2001 Visible-light photocatalysis in nitrogen-doped titanium oxides. *Sci.* **293** (5528), 269–271.

Aware, D. & Jadhav, S. 2016 Synthesis, characterization and photocatalytic applications of Zn-doped TiO_2 nanoparticles by sol–gel method. *Applied Nanoscience* **6** (7), 965–972.

Bapna, K., Phase, D. & Choudhary, R. 2011 Study of valence band structure of Fe doped anatase TiO_2 thin films. *J. Appl. Phys.* **110** (4), 043910.

Burda, C., Lou, Y., Chen, X., Samia, A., Stout, J. & Gole, J. 2003 Enhanced nitrogen doping in TiO_2 nanoparticles. *NANO Lett.* **3** (8), 1049–1051.

Chen, J., Zhong, J., Li, J., Huang, S., Hu, W., Li, M. & Du, Q. 2017 Synthesis and characterization of novel Ag_2CO_3/g-C_3N_4 composite photocatalysts with excellent solar photocatalytic activity and mechanism insight. *Molecular Catal.* **435**, 91–98.

Choi, W. 2006 Pure and modified TiO_2 photocatalysts and their environmental applications. *Catal. Surv. Asia.* **10** (1), 16–28.

Chong, M., Jin, B., Chow, C. & Saint, C. 2010 Recent developments in photocatalytic water treatment technology: a review. *Water Res.* **44** (10), 2997–3027.

Christy, P., Jothi, N., Melikechi, N. & Sagayaraj, P. 2009 Synthesis, structural and optical properties of well dispersed anatase TiO_2 nanoparticles by non-hydrothermal method. *Cryst. Res. Technol.* **44** (5), 484–488.

Dalida, M., Amer, K., Su, C. & Lu, M. 2014 Photocatalytic degradation of acetaminophen in modified TiO_2 under visible irradiation. *Environ. Sci. Pollut. Res.* **21** (2), 1208–1216.

Daneshvar, N., Aber, S., Sayed Dorraji, M., Khataee, A. & Rasoulifard, M. 2007 Photocatalytic degradation of the insecticide diazinon in the presence of prepared nanocrystalline ZnO powders under irradiation of UV-C light. *Sep. Purif. Technol.* **58** (1), 91–98.

Douziech, M., van Zelm, R., Oldenkamp, R., Franco, A., Hendriks, A., King, H. & Huijbregts, M. 2018 Estimation of chemical emissions from down-the-drain consumer products using consumer survey data at a country and wastewater treatment plant level. *Chemosphere* **193** (3–4) 32–41.

Etacheri, V., Di Valentin, C., Schneider, J., Bahnemann, D. & Pillai, S. 2015 Visible-light activation of TiO_2 photocatalysts: advances in theory and experiments. *J. Photochem. Photobiol. C: Photochem. Rev.* **25**, 1–29.

Feng Yao, W., Wang, H., Hong Xu, X., Feng Cheng, X., Huang, J., Xia Shang, S., Na Yang, X. & Wang, M. 2003 Photocatalytic property of bismuth titanate $Bi_{12}TiO_{20}$ crystals. *Appl. Catal. A Gen.* **243** (1), 185–190.

Fiszka Borzyszkowska, A., Pieczyńska, A., Ofiarska, A., Nikiforow, K., Stepnowski, P. & Siedlecka, E. 2016 Bi-B-TiO_2-based photocatalytic decomposition of cytostatic drugs under simulated sunlight treatments. *Sep. Purif. Technol.* **169**, 113–120.

Granberg, R. & Rasmuson, Å. 1999 Solubility of paracetamol in pure solvents. *J. Chem. Eng. Data* **44** (6), 1391–1395.

Gupta, S. & Tripathi, M. 2012 An overview of commonly used semiconductor nanoparticles in photocatalysis. *High Energy Chem.* **46** (1), 1–9.

Halpern, B., Walbridge, S., Selkoe, K., Kappel, C., Micheli, F., D'Agrosa, C., Bruno, J., Casey, K., Ebert, C., Fox, H., Fujita, R., Heinemann, D., Lenihan, H., Madin, E., Perry, M., Selig, E., Spalding, M., Steneck, R. & Watson, R. 2008 A global map

Downloaded from http://iwaponline.com/jwrd/article-pdf/9/1/31/523093/jwrd0090031.pdf
by guest

of human impact on marine ecosystems. *Sci.* **319** (5865), 948–952.

Hamdy, M., Amrollahi, R. & Mul, G. 2012 Surface Ti^{3+}-containing (blue) titania: a unique photocatalyst with high activity and selectivity in visible light-stimulated selective oxidation. *ACS Catal.* **2** (12), 2641–2647.

Huang, S., Lin, Y., Yang, J., Li, X., Zhang, J., Yu, J., Shi, H., Wang, W. & Yu, Y. 2013 Enhanced photocatalytic activity and stability of semiconductor by Ag doping and simultaneous deposition: the case of CdS. *RSC Adv.* **3** (43), 20782.

Huang, Z., Pan, L., Zou, J., Zhang, X. & Wang, L. 2014 Nanostructured bismuth vanadate-based materials for solar-energy-driven water oxidation: a review on recent progress. *Nanoscale* **6** (23), 14044–14063.

Ibhadon, A. & Fitzpatrick, P. 2013 Heterogeneous photocatalysis: recent advances and applications. *Catal.* **3** (1), 189–218.

Ji, T., Yang, F., Lv, Y., Zhou, J. & Sun, J. 2009 Synthesis and visible-light photocatalytic activity of Bi-doped TiO_2 nanobelts. *Mater. Lett.* **63** (23), 2044–2046.

Jones, O., Lester, J. & Voulvoulis, N. 2005 Pharmaceuticals: a threat to drinking water? *Trends in Biotechnol.* **23** (4), 163–167.

Kim, S., Hwang, S. & Choi, W. 2005 Visible light active platinum-ion-doped TiO_2 photocatalyst. *J. Phys. Chem. B* **109** (51), 24260–24267.

Kostich, M., Batt, A. & Lazorchak, J. 2014 Concentrations of prioritized pharmaceuticals in effluents from 50 large wastewater treatment plants in the US and implications for risk estimation. *Environ. Pollut.* **184**, 354–359.

Landmann, M., Rauls, E. & Schmidt, W. 2012 The electronic structure and optical response of rutile, anatase and brookite TiO_2. *J. Phys. Condens. Matter.* **24** (19), 195503.

Lee, J., Mahendra, S. & Alvarez, P. 2010 Nanomaterials in the construction industry: a review of their applications and environmental health and safety considerations. *ACS Nano* **4** (7), 3580–3590.

Li, F., Li, X. & Hou, M. 2004 Photocatalytic degradation of 2-mercaptobenzothiazole in aqueous La^{3+}–TiO_2 suspension for odor control. *Appl. Catal. B: Enviro.* **48** (3), 185–194.

Li, K., Peng, B. & Peng, T. 2016 Recent advances in heterogeneous photocatalytic CO_2 conversion to solar fuels. *ACS Catal.* **6** (11), 7485–7527.

Liu, Z., Sun, D., Guo, P. & Leckie, J. 2007a An efficient bicomponent TiO_2/SnO_2 nanofiber photocatalyst fabricated by electrospinning with a side-by-side dual spinneret method. *NANO Lett.* **7** (4), 1081–1085.

Liu, Z., Sun, D., Guo, P. & Leckie, J. 2007b One-step fabrication and high photocatalytic activity of porous TiO_2 hollow aggregates by using a low-temperature hydrothermal method without templates. *Chem. Eur. J.* **13** (6), 1851–1855.

Liu, F., Lu, L., Xiao, P., He, H., Qiao, L. & Zhang, Y. 2012 Effect of oxygen vacancies on photocatalytic efficiency of TiO_2 nanotubes aggregation. *Bull. Korean Chem. Soc.* **33** (7), 2255–2259.

Luengas, A., Barona, A., Hort, C., Gallastegui, G., Platel, V. & Elias, A. 2015 A review of indoor air treatment technologies. *Rev. Env. Sci. Biotechnol.* **14** (3), 499–522.

Macwan, D., Dave, P. & Chaturvedi, S. 2011 A review on nano-TiO_2 sol–gel type syntheses and its applications. *J. Mater. Sci.* **46** (11), 3669–3686.

Mekki, A., Holland, D., McConville, C. & Salim, M. 1996 An XPS study of iron sodium silicate glass surfaces. *J. Non-Cryst. Solids.* **208** (3), 267–276.

Meng, S., Li, D., Sun, M., Li, W., Wang, J., Chen, J., Fu, X. & Xiao, G. 2011 Sonochemical synthesis, characterization and photocatalytic properties of a novel cube-shaped $CaSn(OH)_6$. *Catal. Commun.* **12** (11), 972–975.

Milićević, B., Đorđević, V., Vuković, K., Dražić, G. & Dramićanin, M. 2017 Effects of Li^+ co-doping on properties of Eu^{3+} activated TiO_2 anatase nanoparticles. *Optical Materials* **72**, 316–322.

Ola, O. & Maroto-Valer, M. 2015 Review of material design and reactor engineering on TiO_2 photocatalysis for CO_2 reduction. *J. Photochem. Photobiol. C Photochem. Rev.* **24**, 16–42.

Park, N., van de Lagemaat, J. & Frank, A. 2000 Comparison of dye-sensitized rutile- and anatase-based TiO_2 solar cells. *J. Phys. Chem. B* **104** (38), 8989–8994.

Patterson, A. 1939 The Scherrer formula for X-ray particle size determination. *Phys. Rev.* **56** 978–982.

Pelaez, M., Nolan, N., Pillai, S., Seery, M., Falaras, P., Kontos, A., Dunlop, P., Hamilton, J., Byrne, J., O'Shea, K., Entezari, M. & Dionysiou, D. 2012 A review on the visible light active titanium dioxide photocatalysts for environmental applications. *Catal. B Environ.* **125**, 331–349.

Pérez, J., Llanos, J., Sáez, C., López, C., Cañizares, P. & Rodrigo, M. 2017 Treatment of real effluents from the pharmaceutical industry: a comparison between Fenton oxidation and conductive-diamond electro-oxidation. *J. Environ. Manage.* **195**, 216–223.

Petrie, B., Barden, R. & Kasprzyk-Hordern, B. 2015 A review on emerging contaminants in wastewaters and the environment: current knowledge, understudied areas and recommendations for future monitoring. *Water Res.* **72**, 3–27.

Qu, Y. & Duan, X. 2013 Progress, challenge and perspective of heterogeneous photocatalysts. *Chem. Soc. Rev.* **42** (7), 2568–2580.

Shimodaira, Y., Kato, H., Kobayashi, H. & Kudo, A. 2006 Photophysical properties and photocatalytic activities of bismuth molybdates under visible light irradiation. *J. Phys. Chem. B* **110** (36), 17790–17797.

Štengl, V. & Bakardjieva, S. 2010 Molybdenum-doped anatase and its extraordinary photocatalytic activity in the degradation of Orange II in the UV and vis regions. *J. Phys. Chem. C* **114** (45), 19308–19317.

Tauc, J. 1970 Absorption edge and internal electric fields in amorphous semiconductors. *Mat. Res. Bull.* **5** (8), 721–729.

Verlicchi, P., Galletti, A., Petrovic, M. & Barceló, D. 2010 Hospital effluents as a source of emerging pollutants: an overview of

Downloaded from http://iwaponline.com/jwrd/article-pdf/9/1/31/523093/jwrd0090031.pdf
by guest

micropollutants and sustainable treatment options. *J. Hydrol.* **389**, 416–428.

Walsh, A., Yan, Y., Huda, M., Al-Jassim, M. & Wei, S. 2009 Band edge electronic structure of BiVO4: elucidating the role of the Bi s and V d orbitals. *Chem. Mater.* **21** (3), 547–551.

Wang, Y., Zhang, L., Deng, K., Chen, X. & Zou, Z. 2007 Low temperature synthesis and photocatalytic activity of rutile TiO_2 nanorod superstructures. *J. Phys. Chem. C* **111** (6), 2709–2714.

Wang, J., Jing, L., Xue, L., Qu, Y. & Fu, H. 2008 Enhanced activity of bismuth-compounded TiO_2 nanoparticles for photocatalytically degrading rhodamine B solution. *J. Hazard. Mater.* **160** (1), 208–212.

Wang, Y., Wang, Q., Zhan, X., Wang, F., Safdar, M. & He, J. 2013 Visible light driven type II heterostructures and their enhanced photocatalysis properties: a review. *Nanoscale* **5** (18), 8326.

Wu, T., Lin, T., Zhao, J., Hidaka, H. & Serpone, N. 1999 TiO_2-assisted photodegradation of dyes. 9. Photooxidation of a Squarylium Cyanine dye in aqueous dispersions under visible light irradiation. *Environ. Sci. Technol.* **33** (9), 1379–1387.

Wu, S., Zhang, L. & Chen, J. 2012 Paracetamol in the environment and its degradation by microorganisms. *Appl. Microbiol. Biotechnol.* **96** (4), 875–884.

Xu, N., Liu, L., Sun, X., Liu, X., Han, D., Wang, Y., Han, R., Kang, J. & Yu, B. 2008 Characteristics and mechanism of conduction/set process in TiN/ZnO/Pt resistance switching random-access memories. *Appl. Phys. Lett.* **92** (23), 232112.

Yang, G., Jiang, Z., Shi, H., Xiao, T. & Yan, Z. 2010 Preparation of highly visible-light active N-doped TiO_2 photocatalyst. *J. Mater. Chem.* **20** (25), 5301.

Yang, J., Wang, X., Dai, J. & Li, J. 2014 Efficient visible-light-driven photocatalytic degradation with Bi_2O_3 coupling silica doped TiO_2. *Ind. Eng. Chem. Res.* **53** (32), 12575–12586.

Yin, M., Li, Z., Kou, J. & Zou, Z. 2009 Mechanism investigation of visible light-induced degradation in a heterogeneous TiO_2/Eosin Y/Rhodamine B system. *Environ. Sci. Technol.* **43** (21), 8361–8366.

Yu, J., Zhang, L., Zheng, Z. & Zhao, J. 2003 Synthesis and characterization of phosphated mesoporous titanium dioxide with high photocatalytic activity. *Chem. Mater.* **15** (11), 2280–2286.

Zhang, L. & Zhu, Y. 2012 A review of controllable synthesis and enhancement of performances of bismuth tungstate visible-light-driven photocatalysts. *Catal. Sci. Technol.* **2** (4), 694.

Zhang, Q., Gao, L. & Guo, J. 2000 Effects of calcination on the photocatalytic properties of nanosized TiO_2 powders prepared by $TiCl_4$ hydrolysis. *J. Appl. Catal. B* **26** (3), 207–215.

Zhang, L., Cheng, H., Zong, R. & Zhu, Y. 2009 Photocorrosion suppression of ZnO nanoparticles via hybridization with graphite-like carbon and enhanced photocatalytic activity. *J. Phys. Chem. C* **113** (6), 2368–2374.

Zhang, L., Wong, K., Yip, H., Hu, C., Yu, J., Chan, C. & Wong, P. 2010 Effective photocatalytic disinfection of E. coli K-12 using AgBr-Ag-Bi_2WO_6 nanojunction system irradiated by visible light: the role of diffusing hydroxyl radicals. *Environ. Sci. Technol.* **44** (4), 1392–1398.

Zhang, J., Zhou, P., Liu, J. & Yu, J. 2014 New understanding of the difference of photocatalytic activity among anatase, rutile and brookite TiO_2. *Phys. Chem. Chem. Phys.* **16** (38), 20382–20386.

Zhao, Z. & Liu, Q. 2008 Designed highly effective photocatalyst of anatase TiO_2 codoped with nitrogen and vanadium under visible-light irradiation using first-principles. *Catal. Lett.* **124** (1–2), 111–117.

Zhong, J., Li, J., Zeng, J., He, X., Huang, S., Jiang, W. & Li, M. 2014 Enhanced photocatalytic activity of In_2O_3-decorated TiO_2. *Appl. Phys. A* **115** (4), 1231–1238.

First received 27 April 2018; accepted in revised form 21 June 2018. Available online 10 July 2018

Downloaded from http://iwaponline.com/jwrd/article-pdf/9/1/31/523093/jwrd0090031.pdf
by guest